High-Temperature Operation of Terahertz Quantum Cascade Laser Sources

Mikhail A. Belkin, *Member, IEEE*, Qi Jie Wang, Christian Pflügl, Alexey Belyanin, Suraj P. Khanna, Alexander Giles Davies, Edmund Harold Linfield, and Federico Capasso, *Fellow, IEEE*

(Invited Paper)

Abstract—Terahertz (THz) quantum cascade lasers (QCLs) are currently the most advanced electrically pumped semiconductor lasers in the spectral range 1–5 THz. However, their operation at room temperature is still an unresolved challenge. In this paper, we discuss our efforts to improve the temperature performance of these devices. In particular, we present THz QCLs that approach thermoelectric cooled operation and discuss factors that limit their high-temperature performance. We also discuss a different type of THz QCL source that produces coherent THz radiation without population inversion across the THz transition. These devices are based on intracavity difference-frequency generation in dual-wavelength mid-IR QCLs, and can now provide microwatt levels of coherent THz radiation up to room temperature. We discuss how the output power of these devices can be further improved to produce milliwatts of THz radiation at room temperature.

Index Terms—Difference-frequency generation, intersubband transitions, nonlinear optics, quantum cascade lasers (QCLs), terahertz (THz) sources.

I. INTRODUCTION

THE terahertz (THz) region (0.3–10 THz) of the electromagnetic spectrum remains one of the least developed spectral regions, despite its proven potential in a number of application areas, including security screening, (bio)chemical detection, remote sensing, nondestructive materials evaluation, communications, astronomy, biology, and medicine. Time-domain THz spectroscopy, based on broadband THz generation using ultrashort pulse Ti-sapphire or fiber lasers in conjunction with suitable photoconverters (such as electrooptic mate-

rials or photoconductive switches), has a demonstrated potential in some of these areas [1], [2]. However, further development of THz systems will require compact semiconductor-based sources: there currently exist no room temperature, high-power, widely tunable THz sources that are suitable for production in large quantities. The power generated by electronic devices (e.g., backward wave oscillators, Gunn and resonant tunneling diode oscillators, and Schottky diode multipliers) is currently well below the milliwatt level for frequencies above 1 THz, because of electron transit time and resistance–capacitance limitations [2], [3]. On the other hand, photonic devices generating THz radiation at room temperature are limited to optically pumped gas lasers, free-electron lasers, and the frequency down-conversion systems that require high-power laser pump source(s) [3]. These photonic devices are either bulky, provide low power output, or can only operate in pulsed mode.

An electrically pumped semiconductor laser, similar to diode lasers in the IR and visible spectral ranges, would be an ideal source for the majority of applications in the THz frequency range. The p-doped germanium hot electron laser was the first electrically pumped semiconductor laser demonstrated at THz frequencies [4]. These devices, however, require a strong magnetic field and liquid helium cooling for operation. The breakthrough occurred in 2002 with the development of THz quantum cascade lasers (QCLs) [5], which followed the demonstration of mid-IR QCLs in 1994 [6]. Currently, THz QCLs have been shown to operate at frequencies from 1 to 5 THz, and can provide more than 100 mW of continuous-wave (CW) THz output power at cryogenic temperatures. THz QCLs have been demonstrated so far in both the AlGaAs/GaAs [5], [7]–[15] and InGaAs/AlInAs [16] material systems. The emission linewidth of distributed-feedback THz QCLs has been measured to be a few tens of kilohertz, which makes these devices ideal local oscillators for heterodyne detection. Such developments of THz QCLs have recently been summarized in a comprehensive review paper by Williams [7].

One of the key desired characteristics for any semiconductor laser is room-temperature operation. This has not been achieved with THz QCLs yet. The highest operating temperatures for these devices are typically achieved for emission frequencies close to 3 THz, which appears to be an optimum frequency for the THz QCL designs demonstrated to date (the reasons for this are discussed in Section III). The timeline for the maximum operating temperatures $T_{\max}$ achieved to date with THz QCLs (in pulsed mode) is shown in Fig. 1(a). As can be seen, the pace of improvements in $T_{\max}$ has slowed down since devices reached
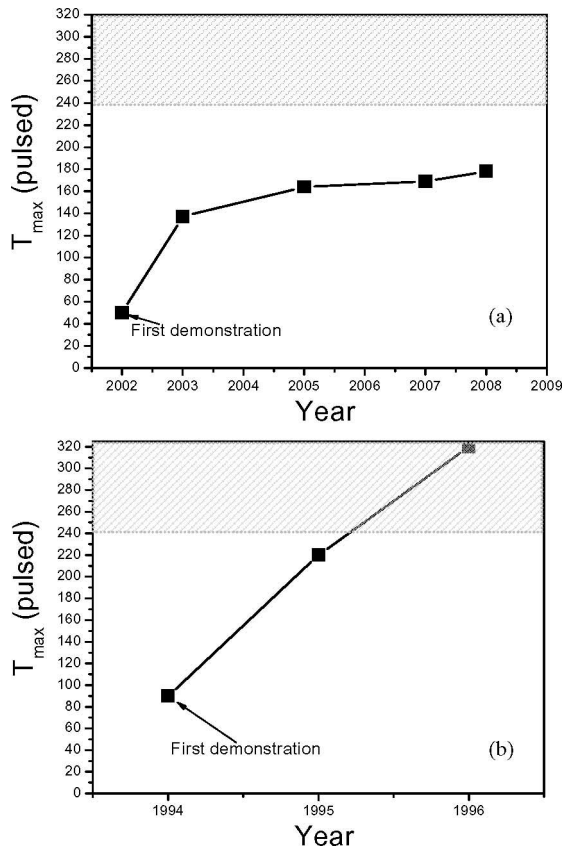
Fig. 1. Timeline for the maximum operating temperature in pulsed mode $T_{\max}$ for THz and mid-IR QCLs since the time of their initial demonstration. (a) THz QCLs. (b) Mid-IR QCLs. The shaded area starts at approximately 240 K, which is a temperature achievable by simple thermoelectric coolers. The data for (a) were taken from [5], [7]–[9], and [12] and that for (b) were taken from [6], [20], and [21].

operating temperatures of $\sim$150 K. Currently, the maximum operating temperatures of THz QCLs continue to increase slowly with improvements in material quality, and in both active region and waveguide designs. In particular, our group recently demonstrated QCLs operating at 3.1 THz with a record operating temperature to date of 178 K [12]. This evolutionary improvement in THz QCL designs may eventually lead to their operation at temperatures above 200 K, which can be accessed with thermoelectric coolers. Nevertheless, it appears from the trend in Fig. 1(a) that a radical design change may be needed to bring the operating temperatures of THz QCLs to room temperature. This might include a dramatic improvement in the active region design of THz QCLs based on GaAs/AlGaAs, or a realization of THz QCLs based on GaN/AlGaN [12], [23], Si/SiGe [24]–[26] or quantum dots systems [27]. We note that, in contrast to THz QCLs, mid-IR QCLs achieved room-temperature operation (in pulsed mode) relatively quickly after their initial demonstration (the timeline for the temperature performance of mid-IR QCLs is plotted in Fig. 1(b), for comparison). Mid-IR QCLs now operate CW well above room temperature [17]–[19].

The problem of creating a room-temperature semiconductor laser as a source of THz radiation can be overcome in a fundamental way, through designing semiconductor THz sources that

do not require population inversion across the THz transition for operation. One way to do this is to produce THz radiation through frequency down-conversion in a nonlinear crystal using IR or visible pump lasers [28]–[30]. This approach offers broad spectral tunability; however, it requires powerful pump lasers and a more complicated optical setup, resulting in bulky and unwieldy sources. We have recently demonstrated that it is possible to integrate monolithically the optical nonlinearity for difference-frequency generation (DFG) into the active region of a dual-wavelength mid-IR QCL [31], [32] using band structure engineering of the QCL active region. The QCL operates at two wavelengths in the mid-IR and produces THz output via intracavity difference-frequency generation. Since mid-IR QCLs have been shown to operate CW with high output powers at and above room temperature [18], [19], this approach can lead to a room-temperature electrically pumped CW THz QCL source.

In this paper, we discuss our efforts to improve the temperature performance of THz QCLs. Only pulsed-mode operation is discussed here. CW operation of these devices depends critically on efficient thermal packaging, which is not the focus of this paper. We note that, with the best thermal packaging demonstrated to date, the maximum CW operating temperature of THz QCLs is approximately 20–50 K below their maximum operating temperature in pulsed mode [7]–[10], [13]–[15].

We start by presenting our results for the GaAs/AlGaAs THz QCLs that have recently achieved operation temperatures up to 178 K (Section II). In Section III, we will then examine the factors that limit the operation of these devices (and THz QCLs in general) at high temperatures. In Section IV, we discuss an alternative approach, based on intracavity difference-frequency generation, to produce room-temperature THz QCL sources, and present the latest results that we have achieved with such devices. Section V then provides a future outlook and conclusions.

II. THz QCLs Operating up to 178 K

The temperature performance of THz QCLs has improved considerably since the initial demonstration of these devices in 2002 [5], as shown in Fig. 1(a). This has stemmed from critical improvements being made in both the active region and waveguide designs.

The waveguide design for THz QCLs is particularly challenging as the optical mode must be strongly confined within the active region to achieve good laser performance. For 1–5 THz radiation, the wavelength of light in the QCL material is between $\sim$20 and 100 μm. It is thus very difficult to confine this radiation in the THz QCL active region because its thickness is limited to $\sim$10 μm, by practical constraints of epitaxial semiconductor growth time. Currently, two types of THz QCL waveguide designs have been demonstrated to address this problem. The first type is the semiinsulating surface-plasmon waveguide [Fig. 2(a)], and this was used in the first THz QCLs [5]. It utilizes a 0.2- to 0.7-μm-thick heavily doped GaAs layer ($n \sim 1$–5×10^{18} cm^{-3}) grown on top of a semiinsulating GaAs substrate with the active region (10–12 μm) grown on top of this layer. A layer of metal is then deposited on top of the active region during the device processing. Such waveguides support a
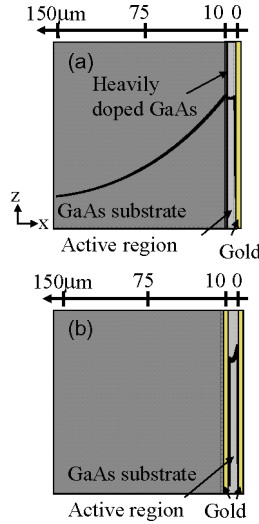
Fig. 2. Schematic representation of (a) the semiinsulating surface-plasmon waveguide and (b) the MM plasmon waveguide used in THz QCLs. The component of the magnetic field of the mode parallel to the layers of the active region (H_y) is plotted.
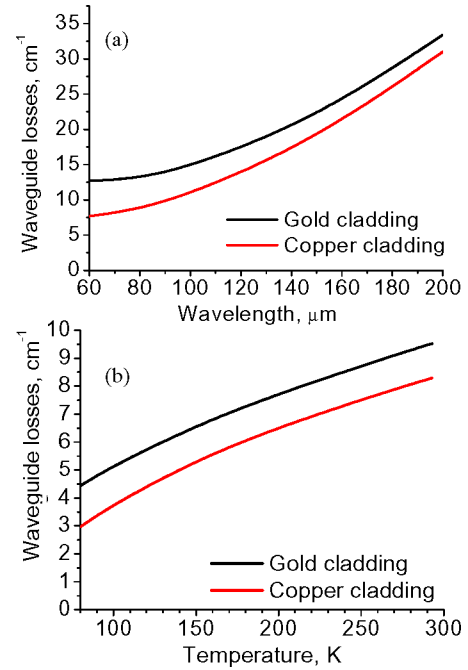

Fig. 3. (a) Calculated waveguide losses in a THz QCL MM waveguide assuming a realistic 10-μm-thick active region design with an average doping of $5 \times 10^{15}\,\mathrm{cm}^{-3}$. We note that long-wavelength, $\lambda > 200\,\mu$m, QCLs typically use lower doped active regions. The data are computed using the optical constants of metals measured at room temperature [35]. (b) Calculated temperature dependence of waveguide losses at 3 THz in a THz QCL MM waveguide assuming a lossless 10-m-thick active region. The data are computed using the optical constants of metals estimated with (1). The data for temperatures below 80 K are very sensitive to the deposited metal quality and are not shown.

surface-plasmon mode bound to the top metal contact and to the lower plasma layer, as shown in Fig. 2(a). This approach leads to a mode confinement factor in the active region in the range $\Gamma = 0.1 - 0.5$. Improvements in the temperature performance of THz QCLs were, however, achieved with the implementation of a second type of waveguide: the metal–metal (MM) design [Fig. 2(b)] [7]–[9], [33]. This waveguide consists of metal films on both sides of the active region, and provides a mode confinement factor of nearly 100%.

In THz QCLs with MM waveguides, 30%–70% of the waveguide losses may originate from the losses associated with the metal claddings, the precise value depending on the emission wavelength, the active region design, and doping [34]. The optical losses in the metal cladding vary according to the type of metal used. In Fig. 3, we compare the calculated waveguide losses for 10-μm-thick, and infinitely wide, MM THz QCL waveguides with claddings made of gold and copper. For the data shown in Fig. 3(a), where the waveguide losses are plotted as a function of wavelength, we consider an active region doped to $5 \times 10^{15}\,\mathrm{cm}^{-3}$, which is a typical average doping level for QCLs emitting between 2 and 5 THz [7]. A 1-D waveguide solver was used for the calculations, and the optical constants for the metals were taken from [35], with the refractive index of the QCL active region being calculated using the Drude–Lorentz approximation with parameters taken from [34].

The optical constants of metals, reported in [35], are quoted at room temperature. To estimate the temperature dependence of the optical constants of copper and gold, we used an approximate expression [36]

$$\mathrm{Re}\,(n) \approx \mathrm{Im}\,(n) \approx \sqrt{\frac{2\pi\sigma}{\omega}} \qquad (1)$$

where $\mathrm{Re}(n)$ and $\mathrm{Im}(n)$ are the real and imaginary parts of the refractive index of a metal, σ is the electrical conductivity of the metal, and ω is the frequency of light. In Fig. 3(b), we plot

the temperature dependence of the optical losses at 3 THz for 10-μm-thick, and infinitely wide, MM waveguides with claddings made of gold and copper, using the optical constants of metals calculated with (1), and the electrical conductivities of copper and gold at different temperatures from [37].

The data in Fig. 3 demonstrate that, by using copper instead of gold, the waveguide losses in MM THz QCL waveguides can be significantly reduced.[1] However, currently gold claddings are typically used in MM waveguides for THz QCLs. Recently, copper-to-copper thermocompression wafer bonding was utilized to fabricate MM waveguides in order to improve the thermal properties of THz QCLs for CW operation [8]. However, the top metal cladding in these devices was still made of gold. To investigate the effect of the waveguide cladding material on the temperature performance of MM THz QCLs, we compared the performance of two sets of devices processed from the same active region material, but with two different MM waveguide cladding metals: gold and copper.

Previously, the best temperature performance was achieved with THz QCLs based on a resonant-phonon design [7]. The active region in our lasers also utilizes the resonant-phonon

---

[1]We also calculated the optical losses for MM THz waveguides with a silver cladding, using data from [35] and [37], and found that the waveguide losses are larger than those in copper metal–metal waveguides. We, however, note that the optical properties of metals in the THz frequency range have not been extensively studied, and vary with temperature, layer deposition quality, metal purity, and other empirical parameters.
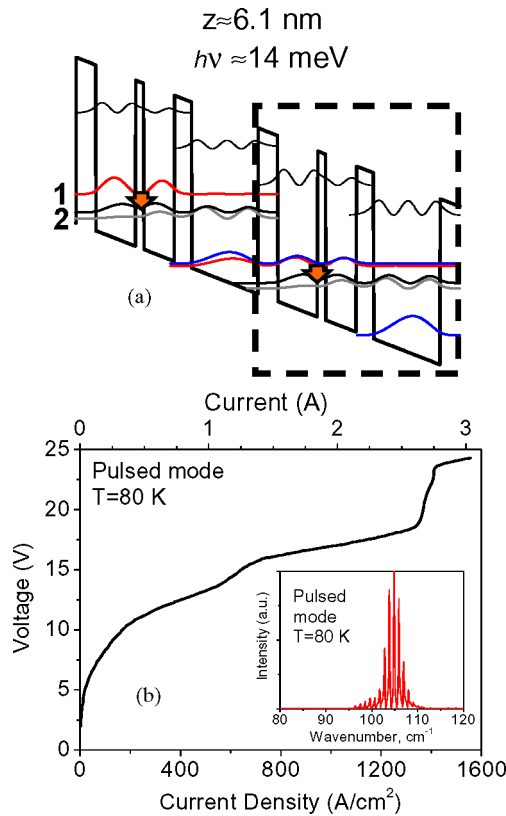
z≈6.1 nm
$h\nu \approx 14$ meV

Fig. 4. (a) Conduction band diagrams of three-quantum-well resonant-phonon active region designs, initially reported in [28]. A single quantum cascade stage is marked by a box. The structure is grown using the GaAs/Al$_{0.15}$Ga$_{0.85}$As material system. The layer sequence, starting from the injection barrier, is **48**/96/**20**/74/**42**/161 Å, with barriers marked in bold. A 55-Å-wide middle section of the 161 Å well is n-doped to 5×10^{16} cm^{-3} and represents the injector region. Laser transitions are shown with arrows. Also shown are the transition dipole moments and emission energies for the laser transitions, calculated for single isolated modules of the structures. (b) $I–V$ characteristic and an emission spectrum (inset) of a 1.3-mm-long and 150-μm-wide device with gold MM waveguide.

Fig. 5. (a) Light intensity–current density ($L–I$) characteristics of the best-performing device with a gold MM waveguide (1.3 mm long and 150 μm wide). Inset: the $L–I$ characteristics of the device close to the maximum operating temperature of 168 K. (b) $L–I$ characteristics of a 1.4-mm-long and 125 μm-wide device with a copper MM waveguide. Inset: the $L–I$ characteristics of the device close to the maximum operating temperature of 178 K. Dips in the $L–I$ characteristics at a current density ∼1150 A/cm^2 are due to some of the laser emission lines coinciding with atmospheric absorption lines. The data in (a) and (b) are not corrected for an estimated 10% power collection efficiency.

design concept and is based on the three-well active region design, initially reported in [11]. The conduction band diagram for the structure is shown in Fig. 4(a). The QCL material was grown by molecular beam epitaxy (MBE) on an undoped GaAs substrate; the growth sequence started with a 250-nm-thick undoped GaAs buffer layer, and was followed by a 300-nm-thick Al$_{0.5}$Ga$_{0.5}$As etch-stop layer, a 75-nm-thick layer of GaAs n-doped to 5×10^{18} cm^{-3}, 226 stages of the active region design with a doping sheet density of $n_s = 2.75 \times 10^{10}$ cm^{-2}, and finally, a 50-nm-thick GaAs layer n-doped to 5×10^{18} cm^{-3}. The material was processed into MM waveguides following the procedure outlined in [12], using either gold or copper for the waveguide cladding. The processed wafers were finally cleaved into approximately 1.5-mm-long bars and indium mounted onto gold-plated copper blocks. Both the gold and copper processing resulted in robust devices that were easy to wire-bond.

Devices were tested in pulsed mode with 30 ns pulses at a 1-kHz repetition rate. Peak powers were measured with a calibrated He-cooled bolometer using two 2 in diameter parabolic mirrors: one with a 5-cm focal length to collect light from the
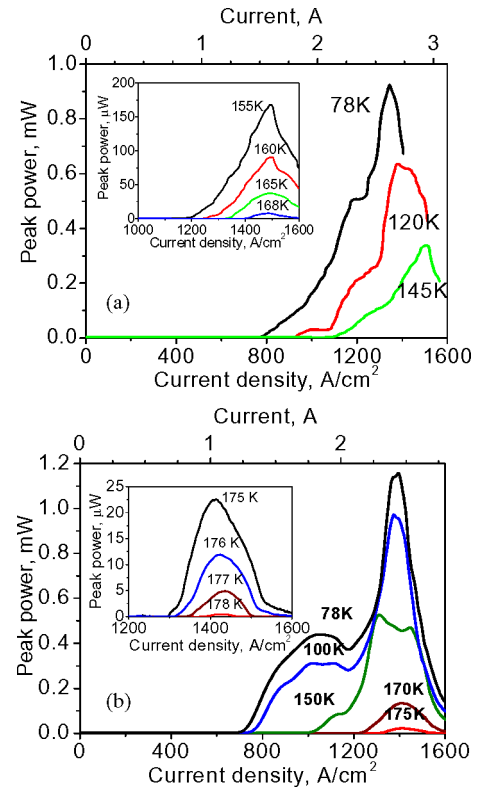
device and the other with a 15-cm focal length to refocus it onto the detector. Fig. 4(b) displays the current density–voltage ($I–V$) characteristic of a representative device with gold cladding layers, as well as a typical emission spectrum. A step in the $I–V$ characteristics at a current density of approximately 700 A/cm^2 can be clearly seen, associated with the injector state aligning with the upper laser state; a second step in the $I–V$ characteristics, at a current density of approximately 1350 A/cm^2, is due to the misalignment of the injector and the upper laser states. Devices processed into MM waveguides with a gold cladding typically operated up to 162–168 K. The light output as a function of current density ($L–I$) for the best performing device with gold MM waveguides, which operated up to 168 K, is shown in Fig. 5(a). Devices processed into MM waveguides with copper cladding typically operated up to 170–178 K. The $L–I$ characteristics for the best-performing device with copper cladding, which operated up to 178 K, is shown in Fig. 5(b).

The maximum operating temperature of 178 K is currently the highest operating temperature achieved in a THz QCL. The active region utilized in our structures was initially reported in [11]. We, however, note that the MM waveguide devices with gold cladding reported in [11] operated only up to 142 K. In contrast, our devices with gold MM waveguides operated up
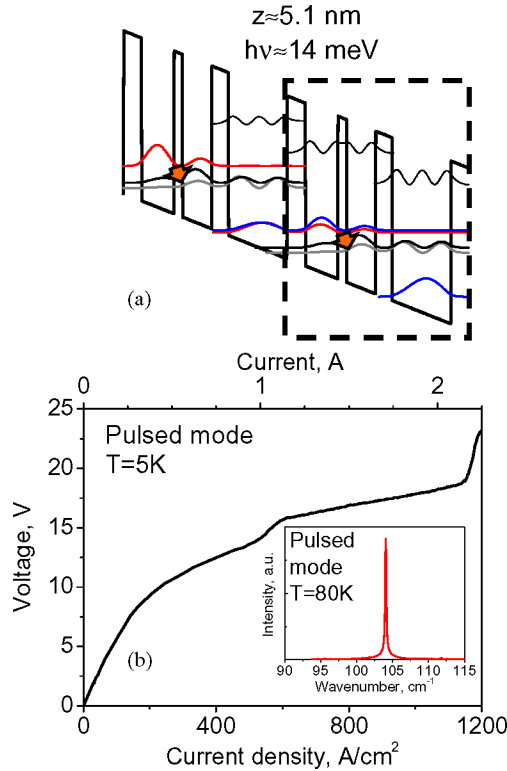
Fig. 6. (a) Conduction band diagrams of the three-quantum-well resonant-phonon active region designs with a diagonal laser transition. A single quantum cascade stage is marked by a box. The structure is grown using the $GaAs/Al_{0.15}Ga_{0.85}As$ material system. The layer sequences, starting from the injection barrier, is **51**/90/**24**/81/**46**/163 Å, with barriers marked in bold. A 57-Å-wide middle section of the 163 Å well is n-doped $5 \times 10^{16} cm^{-3}$. Laser transitions are shown with arrows. Also shown are the transition dipole moments and emission energies for the laser transitions, calculated for single isolated modules of the structures. (b) I–V characteristic and an emission spectrum (inset) of a 1.5-mm-long and 125-μm-wide device with a copper MM waveguide.

to 168 K. The improved performance of our devices may stem from a better growth and/or processing quality. The doping in our structures is also approximately 20% lower than that used in [11]. The record operating temperatures for these THz QCLs were, though, achieved through use of the copper MM waveguide design, which results in a reduction of the waveguide losses. These results establish that a three-well resonant-phonon active region design [11] is a viable alternative to a four-well resonant-phonon active region design [8], and demonstrate that substitution of gold for copper in MM THz QCL waveguides helps to increase the maximum operating temperatures.

In an effort to improve the operating temperatures of THz QCLs further, we designed and tested devices based on the three-quantum-well resonant-phonon active region concept but with a diagonal transition in the active region. The conduction band diagram for the structure is shown in Fig. 6(a). The diagonal laser transition is expected to help improve the electron injection efficiency into the upper laser state, due to the laser transition energy being comparable to the width of the electron distribution in the injector, and reduce the nonradiative electron scattering rate from the upper laser state. These parameters appear to play a critical role in THz QCL performance (as will

be discussed in the next section). However, the diagonal laser transition results in smaller transition dipole moment compared to a vertical transition. In particular, for the structure shown in Fig. 6(a), the calculated dipole moment for the laser transition, $z = 5.1$ nm, is low compared to $z = 6.1$ nm obtained for the vertical transition design [Fig. 4(a)]. Since both structures were designed for an emission energy $h\nu = 14$ meV, the diagonal transition in the structure shown in Fig. 6(a) results in a 30% reduction of the oscillator strength. Because the parameters of the electron transport (injection efficiencies and lifetimes in various laser states) are difficult to estimate theoretically, it is hard to predict whether such diagonal transitions will improve or reduce the temperature performance of the devices.

Experimentally, devices were grown by MBE on an undoped GaAs substrate, keeping the growth parameters as similar as possible to those used for the devices presented in Fig. 4(a); the growth sequence started with a 250-nm-thick undoped GaAs buffer layer, and was followed by a 300-nm-thick $Al_{0.5}Ga_{0.5}As$ etch-stop layer, a 75-nm-thick layer of GaAs n-doped to $5 \times 10^{18} cm^{-3}$, 218 stages of an active region design with a doping sheet density of $n_s = 2.85 \times 10^{10} cm^{-2}$, and finally, a 50-nm-thick GaAs layer n-doped to $5 \times 10^{18} cm^{-3}$. The material was processed into copper MM waveguides and tested in pulsed mode using the setup described previously.

Fig. 6(b) displays the I–V characteristic of a representative device with copper cladding layers, as well as a typical emission spectrum. A step associated with the injector state aligning with the upper laser state can be clearly seen in the I–V characteristics at a current density of approximately 600 A/cm^2; a second step in the I–V characteristics, at a current density of approximately 1100 A/cm^2, is due to the misalignment of the injector and the upper laser states. The position of the second step in the I–V characteristics for the diagonal design occurs at a lower current density than for the vertical design [see Fig. 4(b)]. Considering that both designs have similar doping sheet density and similar anticrossing energies between the states in the injector and the active region (2.0 meV for the upper laser state and 4.3 meV for the lower laser state), this may indicate a more selective injection into the upper laser state and/or a longer upper laser state lifetime in the diagonal design, which would result in lower current densities for a given bias. Devices typically operated up to 170–174 K, which is similar to the maximum operating temperature achieved with the devices based on the vertical transition design. The L–I characteristics for the best-performing device with copper cladding, which operated up to 174 K, are shown in Fig. 7. Overall, it appears that the improvement in the lifetime and injection efficiency associated with the diagonal transition in these devices is negated by the reduced oscillator strength. This results in a temperature performance that is similar to that of devices with vertical transitions [Fig. 5(b)].

III. TEMPERATURE EFFECTS IN THZ QCLS

The dependence of the threshold current density on temperature in our lasers is shown in Fig. 8(a). At low temperatures, the devices reach laser threshold immediately after the band structure is aligned (which is indicated by the steps in the I–V
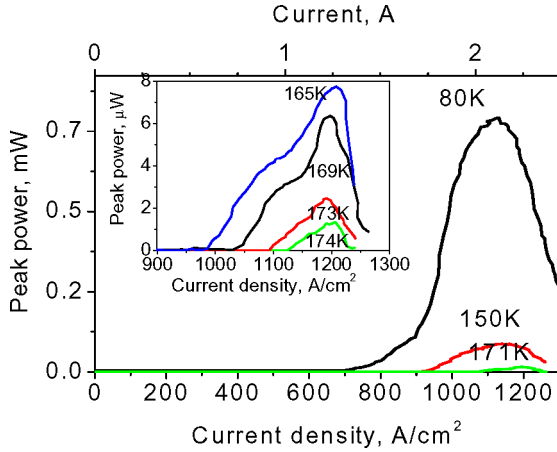
Fig. 7. *L–I* characteristics of the best-performing device with a copper MM waveguide, 1.5 mm long and 125 μm wide. Inset: the *L–I* characteristics of the device close to the maximum operating temperature of 174 K. The data are not corrected for an estimated 10% power collection efficiency.
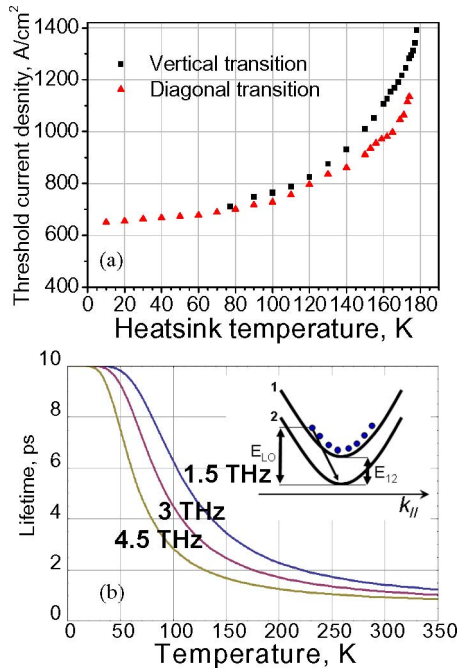

Fig. 8. (a) Threshold current density as a function of temperature for devices based on vertical and diagonal transitions discussed in Section II. Data are shown for devices with copper MM waveguides. (b) Lifetime of the upper laser state versus temperature calculated for THz QCLs with vertical transitions and emission frequencies 1.5, 3, and 4.5 THz using (4) and assuming $\tau_{1,\mathrm{hot}} = 0.5$ ps and $\tau_{1,\mathrm{cold}} = 10$ ps. Inset: schematic representation of the process of longitudinal optical (LO) phonon scattering of thermally excited electrons from state 1 to state 2.

curves). At higher temperatures, the threshold current density is determined by the temperature dependence of the laser transition parameters such as lifetimes of the upper and lower laser states, and the injection efficiency. The lasing ceases and the devices go into the negative differential resistance regime at current densities of $\sim$1300 A/cm^2 for the devices with a vertical laser transition, and $\sim$1000A/cm^2 for the devices with a diagonal laser transition, which indicates loss of band alignment.

Typically, Monte Carlo simulations are used to model the electron transport and lasing condition in THz QCLs as a function of temperature [38]–[42]. Here, we attempt to explain the dependence of the threshold current density on temperature qualitatively, with a simple physical picture. We assume that, under the operating bias, electrons are injected either into the upper laser state ("state 1") with injection efficiency η or into the lower laser state ("state 2") with injection efficiency $(1-\eta)$ [see Figs. 4(a) and 6(a)]. The laser gain g in our structures can then be written as

$$g = \sigma \Delta N = \sigma \frac{J}{q_0} \left(\tau_1 \eta \left(1 - \frac{\tau_2}{\tau_{12}} \right) - (1 - \eta) \tau_2 \right) \quad (2)$$

where J is the current density, τ_1, τ_2 are the lifetimes of the upper and lower laser states, respectively, σ is the laser transition cross section, q_0 is the electron change, and τ_{12} is the relaxation time between states 1 and 2.

The lifetime of the lower laser state (τ_2) is determined by the electron extraction time through the extraction barrier into the injector [the doped wells in Figs. 4(a) and 6(a)] and is not expected to display a strong temperature dependence. The lifetime of the upper laser state (τ_1) is, however, expected to change significantly with temperature. At low temperatures, the lifetime τ_1 is relatively long, 5–10 ps or higher, and is determined by electron–electron, electron–impurity, and interface roughness scattering [43]–[45]. At higher temperatures, however, the electrons in state 1 can acquire sufficient in-plane momentum and be efficiently scattered to state 2 via longitudinal optical (LO) phonon scattering [7], [43], [44]. The mechanism of this process has been discussed in [7] and is shown schematically in Fig. 8(b). For the THz QCLs with an active region based on vertical transitions, such scattering can be extremely efficient as the difference between the electron momenta in the initial and final electron states is small and comparable to the inverse of the active region length

$$q_{12} \approx \sqrt{2m^* \frac{E_{\mathrm{LO}} - E_{12}}{\hbar^2}} \approx 0.2 \ \mathrm{nm}^{-1} \quad (3)$$

where we assume $E_{\mathrm{LO}} = 36$ meV, $E_{12} = \hbar\omega \approx 14$ meV, and $m^* \approx 0.07m_0$. For such small values of q_{12}, the lifetime of the thermally excited electrons in the upper laser state in our structures is $\tau_{1,\mathrm{hot}} \approx 0.5$ ps in accordance with the lifetimes calculated and measured for resonant optical phonon scattering in quantum wells [43], [44]. To estimate the lifetime of the electron ensemble in the upper laser state, we assume that the electron energy distribution follows a 2-D Fermi–Dirac distribution, and obtain for the lifetime of the upper laser state (τ_1)

$$\tau_1 = N_1 \left(\frac{N_{1,\mathrm{cold}}}{\tau_{1,\mathrm{cold}}} + \frac{N_{1,\mathrm{hot}}}{\tau_{1,\mathrm{hot}}} \right)^{-1} \quad (4)$$

where $N_{1,\mathrm{cold}}$ ($N_{1,\mathrm{hot}}$) are the electron densities in state 1 with $E_{//} + \hbar\omega < E_{\mathrm{LO}}$ ($E_{//} + \hbar\omega \geq E_{\mathrm{LO}}$), $N_1 = N_{1,\mathrm{cold}} + N_{1,\mathrm{hot}}$, and we assume that the optical phonon scattering of thermally excited electrons from state 1 to state 2 determines the lifetime of state 1 (i.e., $\tau_1 \approx \tau_{12}$). The lifetimes of the upper laser state calculated using (4) for THz QCLs with various emission frequencies are shown in Fig. 8(b). For these calculations, we

assumed that the lifetime of the "hot" electrons $\tau_{1,\text{hot}} = 0.5$ ps and that of the "cold" electrons $\tau_{1,\text{cold}} = 10$ ps. The data show a dramatic reduction of the upper laser state lifetime with temperature. We note that the electron temperatures in the upper laser state in THz QCLs were simulated [38] and measured [46] to be approximately 50–100 K above that of the lattice temperature. Thus, the upper laser state lifetime in our devices at room temperature is expected to be below 1 ps. Other THz QCLs with vertical or nearly vertical laser transitions are expected to have similar upper laser state lifetime dependences on temperature.

The lifetime of the lower laser state (τ_2) in our structures is determined by resonant tunneling into the injector. The precise value of τ_2 may be difficult to estimate as it requires knowledge of the electron scattering (dephasing) time. However, most theoretical reports that have modeled the transport in resonant-phonon-based THz QCLs put the value for τ_2 in the range 0.5–1 ps when the extraction barrier thickness is similar to that in our structures [39], [41], [42]. Thus, the value of τ_2 is comparable to the upper laser state lifetime $\tau_1 \approx \tau_{12}$ at high temperatures.

From (2), we can see that as the lifetime of the upper laser state $\tau_1 \approx \tau_{12}$ approaches that of τ_2, the laser gain approaches zero. Equation (2) also shows that the injection efficiency η plays a critical role in determining the temperature performance of the devices. We have simulated the dependence of the threshold current density on temperature, assuming various values for τ_2 and the injection efficiency, for a 1.4-mm-long and 125-μm-wide device based on a vertical transition, with a copper MM waveguide. [The experimental data from this device are shown in Fig. 5(b).] The threshold gain was calculated to be ≈ 12 cm^{-1} using the data in Fig. 3(a) and assuming 80% facet reflectivity [34]. The transition cross section σ was estimated assuming a value of 5 meV for the emission linewidth (full-width at half-maximum) of our lasers at high temperatures. The results of the simulation for different values of τ_2 and η are shown in Fig. 9(a). In Fig. 9(b), we compare the measured temperature dependence of the threshold current density [shown in Fig. 8(a)] with the simulated curve obtained using (2) and assuming $\tau_2 = 0.7$ ps and $\eta = 0.665$. We note that, at low temperatures, the threshold current density is determined by the band structure alignment, and devices reach the lasing threshold immediately after the band structure is properly aligned [which is indicated by the step in their I–V characteristics—see, for example, Fig. 4(b)].

The aforementioned mechanism for the decline in laser gain with temperature appears to be fairly universal and applicable to any THz QCLs based on a vertical laser transition. Quantitatively, the model is accurate only if electron thermalization in the upper laser subband occurs much faster than optical phonon scattering. If the thermalization and LO phonon emission times are of the same order (which may be the case for THz QCLs with relatively low electron densities), the electron distribution becomes depleted at high energies above $E_{//} = E_{\text{LO}} - \hbar\omega$, which leads to the reduction in $N_{1,\text{hot}}$ compared to the result obtained using the Fermi–Dirac distribution. Therefore, the decrease in the upper state lifetime with temperature may not be as dramatic, as shown in Fig. 8(b).

While the simple description of electron transport based on (2) and (4) provides only a qualitative picture, the results shown
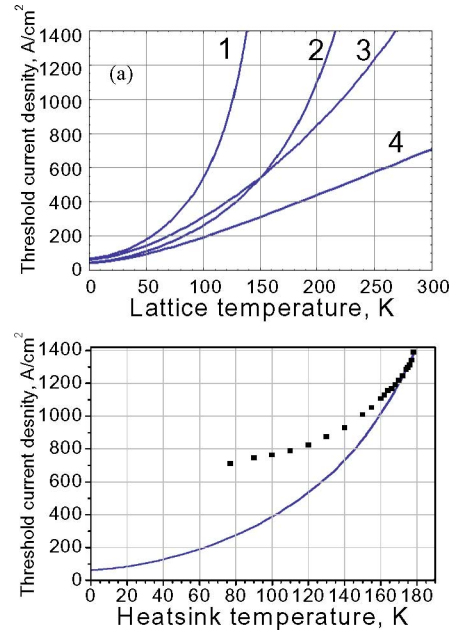

Fig. 9. (a) Threshold current density as a function of lattice temperature calculated using (2) and assuming: 1) $\tau_2 = 1$ ps, $\eta = 0.7$; 2) $\tau_2 = 1$ ps, $\eta = 1$; 3) $\tau_2 = 0.5$ ps, $\eta = 0.7$; and 4) $\tau_2 = 0.5$ ps, $\eta = 1$. The electron temperature in these simulations is assumed to be 50 K above the lattice temperature. (b) Experimental dependence of the threshold current density on temperature (squares) for our QCLs based on the vertical laser transition, overlapped with the simulated curve obtained using (2) and assuming $\tau_2 = 0.7$ ps, $\eta = 0.665$ (line).

in Fig. 9 underline the challenge of achieving room-temperature operation with GaAs/AlGaAs THz QCLs. It shows that devices would need to have a nearly 100% injection efficiency into the upper laser state, and extremely short extraction lifetime from the lower laser state, to be able to operate at room temperature. The data in Fig. 9 also show that our devices would achieve higher operating temperatures had they been able to operate at higher current densities without losing their proper bandstructure alignment. This can be achieved through increasing the doping and reducing the thickness of injection and extraction barriers. However, an increase of doping results in an increase of the waveguide losses [47], [48], and a reduction of the thickness of the injection and extraction barriers results in emission linewidth broadening, a reduced lifetime of the upper laser state, and a poor injection efficiency [49], [50]. In fact, because the QCL electron transport and lasing is difficult to model accurately, the injection and extraction barriers in our devices, as well as the doping, were optimized empirically to achieve designs with the highest possible T_{max} [49], [50].

We note that at high temperatures, the electron lifetime in the upper laser state in our devices (≤ 1 ps) is comparable to the upper laser state lifetime of long-wavelength ($\lambda \sim 15\,\mu$m) mid-IR QCLs. Eventually, the latter devices did achieve room-temperature operation (in pulsed mode) through utilizing two-phonon resonance and bound-to-continuum designs that resolved "the electron extraction bottleneck" [51]. However, the situation with THz QCLs is more complicated as it is also very difficult to achieve selective injection of electrons into the upper laser state when the upper and lower lasers states are separated
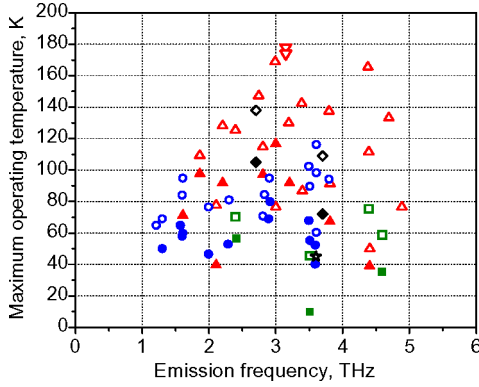
Fig. 10. Summary of the maximum operating temperatures of THz QCLs reported to date. Solid symbols refer to CW operation, and open symbols refer to pulsed operation. Circles refer to bound-to-continuum designs, green squares are chirped superlattice designs, upside triangles are resonant-phonon designs, diamonds are double-resonant-phonon depopulation designs [10], and the black star is a bound-to-continuum THz QCL reported in the In-GaAs/AlInAs materials system [16]. Red upside-down triangles represent the results discussed in this paper. The data are taken from [7], [10], [12], [15], and [16].

by only 4–20 meV (1–5 THz). Moreover, adding more electron states in the THz QCL active region or injector results in a reduction of the maximum current density in the QCL structure (for a given doping), linewidth broadening, and/or parasitic intersubband absorption of the THz radiation. As a result, the bound-to-continuum [13]–[15] and two-phonon resonance [10] THz QCLs designs tested so far have not achieved operating temperatures as high as those obtained with simpler resonant-phonon designs. This is illustrated in Fig. 10, where a summary of the temperature performance of THz QCLs demonstrated to date by different groups is shown. The record operating temperature of 178 K at 3 THz was achieved with the devices described in the previous section, and the maximum operating temperatures of THz QCLs tend to be lower for devices operating at frequencies both higher and lower than ~3 THz. The high-frequency trend can be explained by the fast reduction of the upper laser state lifetime with temperature [see Fig. 8(b)] and the increase of the waveguide losses due to the onset of the phonon absorption band (*Reststrahlenband*). The reduction of the maximum operating temperatures of THz QCLs at low frequencies is likely to be a result of the reduction of injection efficiency into the upper laser state, and the increase of the waveguide losses due to free-carrier absorption.

Different approaches may be utilized to improve the temperature performance of THz QCLs [7], including improving the active region designs for existing GaAs/AlGaAs or InGaAs/AlInAs THz QCLs, utilizing new materials systems, and using 0-D heterostructures. In particular, the GaN/AlGaN system has been suggested, because its large LO-phonon energy (about 90 meV) would present a high barrier to thermally activated optical phonon scattering [22], [23]. Alternatively, using 0-D heterostructures would allow suppression of thermally activated optical phonon scattering processes in the upper laser level and provide high injection efficiency into the upper laser level [27]. It is, however, important to recognize that the

GaAs/AlGaAs material system used for the current state-of-the-art THz QCLs is one of the best in terms of the superlattice quality, which is extremely important for THz QCLs because the upper and lower energy levels are closely spaced. No operational QCLs have yet been reported at any wavelength in either GaN/AlGaN or quantum-dot-based systems.

The problem of creating a room-temperature semiconductor laser source of THz radiation can also be overcome in a fundamental way through designing semiconductor THz sources that do not require population inversion across the THz transition for operation. One way to achieve this is to produce THz radiation via frequency down-conversion in a nonlinear crystal using IR or visible pump lasers [28]–[30]. We have recently demonstrated that it is possible to integrate monolithically a giant optical nonlinearity into an active region of a dual-wavelength mid-IR QCL [31], [32]. Since mid-IR QCLs have been shown to operate CW with high output powers at and above room temperature [18], [19], this approach can lead to a room-temperature electrically pumped CW THz QCL source, based on intracavity DFG in mid-IR QCLs. In the next section, we will describe the design, current performance, and perspectives of such devices.

IV. THz QCL Sources Based on Intracavity DFG

DFG is a nonlinear optical process in which two beams at frequencies ω_1 and ω_2 interact in a medium with effective second-order nonlinear susceptibility $\chi^{(2)}$ to produce radiation at frequency $\omega = \omega_1 - \omega_2$. The intensity of the latter is given by the expression [28], [31], [52]

$$W(\omega = \omega_1 - \omega_2) = \frac{\omega^2}{8\varepsilon_0 c^3 n(\omega_1)n(\omega_2)n(\omega)} \left| \chi^{(2)} \right|^2$$
$$\times \frac{W(\omega_1)W(\omega_2)}{S_{\text{eff}}} \times l_{\text{coh}}^2 \qquad (5)$$

where $l_{\text{coh}} = 1/(|\vec{k} - (\vec{k}_1 - \vec{k}_2)|^2 + (\alpha/2)^2)$ is the coherence length, $W(\omega_i)$, $n(\omega_i)$, and $\vec{k}_i$ are the power, refractive index, and the real wave vector of the beam at frequency ω_i, respectively, α represents the losses at the DFG frequency, and S_{eff} is the effective area of interaction. It follows from (5) that, for efficient DFG, one needs to use materials with large $\chi^{(2)}$, input beams of high intensity, and achieve low losses and phase matching $|\vec{k} - (\vec{k}_1 - \vec{k}_2)| \approx 0$. For intracavity THz DFG in an electrically pumped semiconductor laser, the intensities of the pump beams are limited to ~10 MW/cm^2 and l_{coh} is limited to hundreds of micrometers by free-carrier absorption at the THz frequencies. Under these circumstances, it is only possible to achieve efficient THz DFG if $\chi^{(2)}$ in the laser is orders of magnitude larger than that in typical nonlinear crystals [28], [31].

Quantum well structures with giant optical nonlinearities in the mid- and far-IR can be engineered by tailoring optical transitions within the same band, i.e., making use of intersubband transitions [53]–[57]. In particular, a coupled quantum well structure with $\chi^{(2)} = 10^6$ pm/V for DFG at 60 μm was reported in [56], four orders of magnitude larger than that of traditional nonlinear crystals (LiNbO$_3$, GaP, GaAs, etc.) [28]. In principle, such a
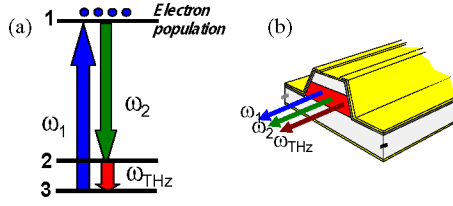
Fig. 11. (a) Schematic diagram of the THz DFG process with population inversion. (b) Schematic view of the THz source based on intracavity DFG in a dual-wavelength mid-IR QCL. The active region generates light output at mid-IR frequencies ω_1 and ω_2 through the laser action, and light output at a THz frequency ω_{THz} through the DFG process.

Fig. 12. (a) Calculated conduction band diagram of one period of a "bound-to-continuum" QCL section at applied bias of 37 kV/cm. (b) "Two-phonon resonance" QCL section at applied bias of 35 kV/cm. The wavy curves represent the moduli squared of the wavefunctions. The electron states in the "bound-to-continuum" section important for DFG are shown in bold and labeled 1– 3. They correspond to levels 1, 2, and 3 shown in the DFG schematics in Fig. 11(a). The layer sequence (in angstrom), starting from the injection barrier, for the "bound-to-continuum" section is **40**/20/**7**/60/**9**/59/**10**/52/**14**/38/**12**/32/**12**/32/**16**/31/**19**/31/**22**/30/**22**/29. The layer sequence for one period of a "double-phonon resonance" section is **40**/24/**7**/65/**8**/64/**8**/58/**22**/40/**13**/38/**14**/37/**15**/36/**19**/36/**25**/36/**25**/35. The barriers are indicated in bold face and the underlined layers are doped to $n = 3 \times 10^{17} \text{cm}^{-3}$.

large value of $\chi^{(2)}$ would enable efficient THz generation even for relatively low pump intensities and relatively short coherence lengths. However, high optical nonlinearity in these structures is achieved because all interacting fields are in resonance with the intersubband transitions. This results in strong absorption of the pump and THz DFG beams, and unavoidably limits THz DFG efficiency. The problem can be solved by designing an active nonlinear semiconductor device with the coupled quantum well states providing both laser gain and giant $\chi^{(2)}$. In this case, instead of resonant absorption of the pump frequency, one has laser gain. Intrawaveguide generation of all interacting fields provides their tightest possible confinement and overlap, as reported for second-harmonic generation in QCLs [52]. A schematic diagram of this DFG process is shown in Fig. 11.

We have studied ways to incorporate a giant $\chi^{(2)}$ into mid-IR QCL designs that are known to produce high output powers and work at room temperature. We realized that a bound-to-continuum mid-IR QCL design [51] intrinsically possesses strong optical nonlinearity for THz DFG, and these devices can be further optimized. The QCL active region in our devices is composed of two substacks. The first substack consists of stages of a "bound-to-continuum" QCL structure with a laser emission wavelength of 8.9 μm and a giant $\chi^{(2)}$ for THz DFG [Fig. 12(a)]. The second substack consists of stages of a "two-phonon resonance" QCL structure [51] with a laser emission wavelength of 10.5 μm and a relatively small $\chi^{(2)}$ for DFG [Fig. 12(b)].

Our devices were grown by MBE using $In_{0.53}Ga_{0.47}As/In_{0.52}Al_{0.48}As$ heterostructures, with upper InP waveguide cladding regrown by metal–organic chemical vapor deposition (MOCVD). The MBE growth started on an InP substrate, n-doped to $9 \times 10^{16} \text{cm}^{-3}$, with 30 stages of the "double-phonon resonance" active region, designed to emit at 10.5 μm, followed by a 100-nm-thick GaInAs spacer, n-doped to $3 \times 10^{16} \text{cm}^{-3}$, and 30 stages of the "bound-to-continuum" active region, designed to emit at 8.9 μm. The conduction band diagrams for the two sections are shown in Fig. 12, with the layer sequences for the two sections also listed. The MBE growth ended with a 50-nm-thick GaInAs layer, n-doped to $3 \times 10^{16} \text{cm}^{-3}$. An upper waveguide cladding, consisting of 3.5-μm-thick and 0.2-μm-thick InP layers, n-doped to $5 \times 10^{16} \text{cm}^{-3}$ and $5 \times 10^{18} \text{cm}^{-3}$, respectively, was then overgrown by MOCVD.

The bound-to-continuum section in our devices is expected to have the largest $\chi^{(2)}$ for DFG. For resonant DFG, the expression
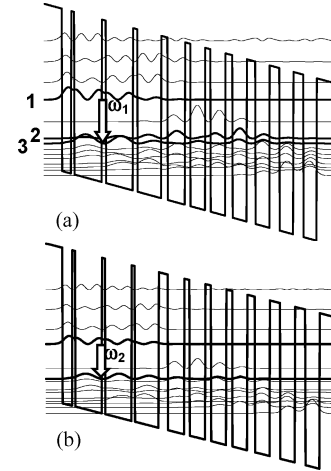
for the nonlinear susceptibility [28], [31] simplifies to

$$\chi^{(2)}\left(\omega = \omega_1 - \omega_2\right) \approx \frac{e^3}{\hbar^2 \varepsilon_0} \frac{z_{12} z_{23} z_{31}}{(\omega_3 - \omega_{23} + i\Gamma_{23})}$$
$$\times \left(\frac{N_1 - N_3}{(\omega_1 - \omega_{13} + i\Gamma_{31})} + \frac{N_1 - N_2}{(-\omega_2 + \omega_{12} + i\Gamma_{21})} \right) \quad (6)$$

where N_i are the population densities in the electron states $i = 1, 2$, and 3 [see Fig. 11], and ez_{ij}, ω_{ij}, and Γ_{ij} are the dipole matrix element, frequency, and broadening of the transition between states i and j, respectively. Assuming $N_2 \approx N_3$ for simplicity, both population differences in (6) are equal to the population inversion density ΔN_e that can be determined from a "gain = loss" condition. The laser gain in a medium with population inversion is given by an expression [28]

$$g\left(\omega_1\right) \approx \frac{\omega_1}{cn_{\text{eff}}\left(\omega_1\right)} \frac{\Delta N_e e^2}{\varepsilon_0 \hbar} \sum_n \frac{|z_{1n}|^2}{(\omega_1 - \omega_{1n}) + i\Gamma_{1n}} \quad (7)$$

where $n_{\text{eff}}(\omega_1)$ is the effective refractive index of the laser mode and n refers to the lower laser levels. The "gain = loss" condition for a QCL is [57]

$$g_{\max} \times \Gamma = \alpha_{wg} + \alpha_m \quad (8)$$

where $g_{\max}$ is the peak of the laser gain in (7), Γ is a modal overlap factor with an active region, and α_{wg} and α_m are waveguide and mirror losses, respectively. We estimate for our devices $\Gamma \approx 0.4$, $\alpha_{wg} \approx 8 \text{ cm}^{-1}$, and $\alpha_m \approx 3 \text{ cm}^{-1}$ and obtain that $g_{\max} \approx 28 \text{ cm}^{-1}$. Assuming $\Gamma_{ij} \approx 7.5$ meV, we obtain from (6)–(8) that $\Delta N_e \approx 2 \times 10^{15} \text{ cm}^{-3}$ and $|\chi^{(2)}| \approx 4 \times 10^4$ pm/V for the DFG process in our devices.
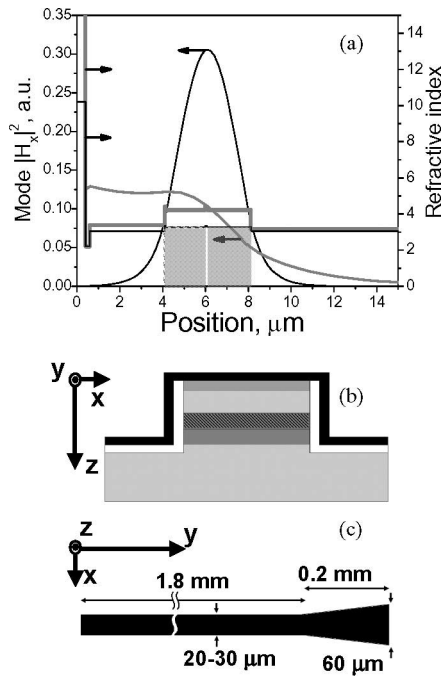
Fig. 13. (a) Magnetic field intensity in the TM_{00} waveguide mode (left axis) and the refractive index profile (right axis) for $\lambda = 8.9$ μm (thin black line) and $\lambda = 60$ μm (thick gray line). Also shown in gray are the two sections of the active region. A section with high optical nonlinearity is shaded. (b) Waveguide structure: the gold layer is shown in black, the insulating Si_3N_4 layer is in white, and the semiconductor is in gray (for low-doped InP layers) and dark gray (for a high-doped InP layer and the two active region sections). The bound-to-continuum section has the darkest shade. (c) Ridge waveguide shape, viewed from top: the back facet (left side) has a HR coating.

A critical issue in achieving high THz output power in our devices is the waveguide design. The waveguide must provide low-loss dielectric mode confinement for the mid-IR pump beams, and also good mode confinement and relatively low loss for the THz wave generated through DFG. In addition, the waveguide design must allow for phase matching in the DFG process $|\vec{k} - (\vec{k}_1 - \vec{k}_2)| \approx 0$. The waveguide used in our devices was designed to satisfy both requirements and is shown in Fig. 13. To reduce the losses for the THz radiation, we used low doping in the active region and waveguide layers. The thickness and doping of the waveguide cladding layers were also tailored to provide the effective refractive indexes for the mid-IR and THz modes to achieve phase matching for the intracavity THz DFG process. The calculated waveguide modes for mid-IR and THz waves, along with the waveguide refractive index profile, are shown in Fig. 13(a). Using the effective refractive indexes calculated for the TM_{00} modes of mid-IR pump beams and the THz wave, as well as the THz mode losses, we estimate the coherence length [see (5)] in our devices to be approximately 50–80 μm for 25- to 60-μm-wide ridges. The limiting factor for l_{coh} in our case is the THz waveguide loss, which is calculated to be $\alpha \approx 250$ cm^{-1}. We note that α can be reduced to below 100 cm^{-1} through further reduction of the doping in the substrate, waveguide layers, and active region.

The laser material was processed into deep-etched ridge waveguides, 2-mm-long and 25-μm-wide, tapered to 60 μm to-

ward the front facet, with a 400-nm-thick Si_3N_4 insulating layer on the lateral walls of the ridge and a Ti/Au (20 nm/400 nm) top contact [see Fig. 13(b) and (c)]. A nonalloyed Ge/Au contact was deposited on the back of the wafer. A high-reflectivity coating, consisting of Al_2O_3/Au (200 nm/50 nm) layers, was evaporated on the back facet of the devices. Tapering was introduced in order to improve the outcoupling efficiency of THz radiation from the waveguide [34].

For measurements, devices were operated in pulsed mode with 60 ns pulses at a 250-kHz repetition rate. Radiation was collected using two 2-in-diameter parabolic mirrors: one with a 5-cm focal length to collect light from the device and the other with a 15-cm focal length to refocus it onto a thermopile or mercury–cadmium–telluride (MCT) detector for mid-IR measurements, or an He-cooled calibrated Si bolometer for THz measurements. Mid-IR powers were corrected for the 70% collection efficiency of the apparatus. Spectra were taken with a Fourier transform IR spectrometer. For THz measurements, mid-IR radiation was blocked using optical filters. Our devices operated at dual wavelength up to room temperature. The current–voltage characteristic, the dependence of the product of the two mid-IR pump powers, $W(\omega_1) \times W(\omega_2)$, on current, and an emission spectrum for a typical device are shown in Fig. 14(a).

Because of the subwavelength THz mode confinement in the waveguide [see Fig. 13(a)], the THz DFG output from our devices is expected to be strongly divergent and THz outcoupling efficiency may be poor [34], [59]. Recently, it has been demonstrated that an Si hyperhemispherical lens, attached to the device facet, may help to resolve these problems [59]. We have equipped selected devices with 2-mm-diameter, 1.19-mm-height high-resistivity Si hypersemispherical lenses. The lenses were positioned to within 5 μm of a device facet, following a procedure similar to that in [59]. For lens alignment, we imaged the mid-IR output from our devices with an MCT detector. Devices with a lens demonstrated a 25-fold increase in collected THz DFG power output, compared to devices without a lens. The increase stems from improved collection efficiency (from an estimated 10% to nearly 100%) and improvements in the THz outcoupling efficiency. A typical THz emission spectrum at 80 K of a device with a lens is shown in Fig. 14(b). The THz DFG spectra of the same device, collected at different temperatures, are shown in Fig. 14(c). THz output was observed up to room temperature, with THz power decreasing from approximately 7 μW at 80 K to approximately 300 nW at room temperature. This trend is illustrated in Fig. 14(d), where we have also plotted the product of the mid-IR pump powers at different temperatures. The data in Fig. 14(d) indicate that a drop in THz output power originates mostly from a decrease in the mid-IR pump powers [see (1)], while THz DFG conversion efficiency remains approximately constant at $\sim$5 μW/W^2.

The coherence length in the devices reported before is limited to $\sim$80 μm by the free-carrier absorption at THz frequencies. Devices with reduced doping and improved waveguide design may achieve l_{coh} up to several hundreds of micrometers. However, a typical length for a QCL waveguide is 2–5 mm. Thus, most of the THz light generated via intracavity DFG in the
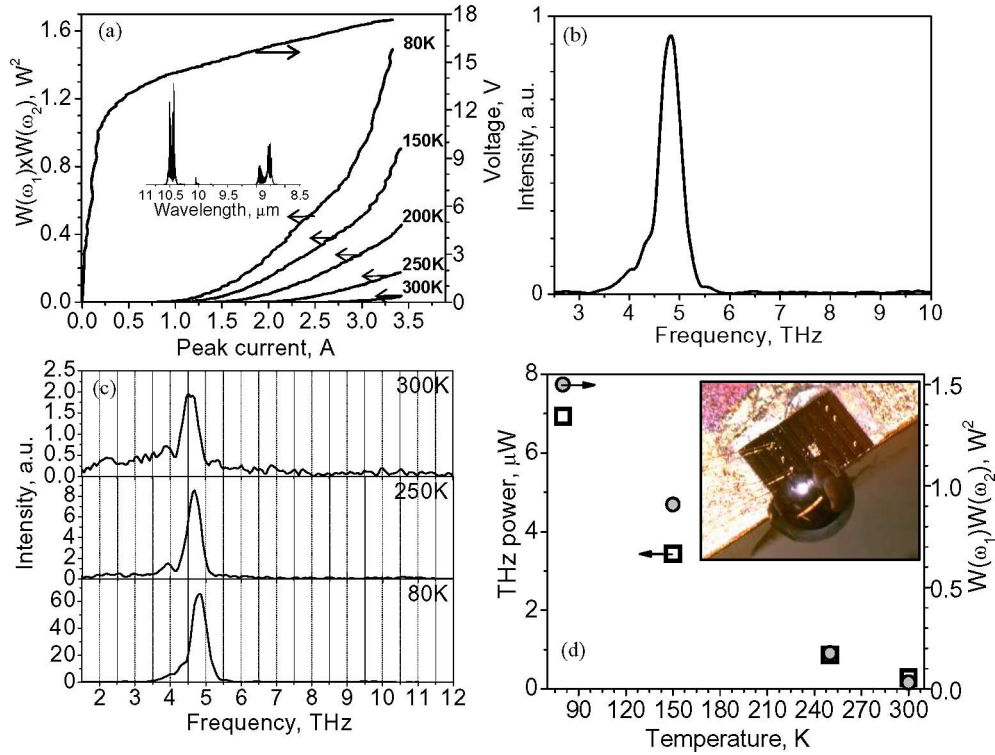
Fig. 14.   (a) Product of the mid-IR pump intensities (left axis) as a function of current and current–voltage (right axis) characteristics of a representative device. Inset: mid-IR emission spectrum of the device at 80 K. (b) THz emission spectra of a device with an Si hyperhemispherical lens attached to the facet, measured at 80 K. (c) THz emission spectra of the same device measured at different temperatures. (d) Temperature dependence of the measured THz DFG signal intensity (right axis) and the product of mid-IR pump powers for a device with an Si lens. Inset: photograph of a device with an Si lens attached to a facet. The measurements in (d) and all the spectral measurements were done with a device operated with 3.5 A current pulses.

edge-emitting THz QCL sources based on intracavity DFG devices is lost due to free-carrier absorption. This problem can be avoided if the THz radiation is extracted vertically from the whole length of the waveguide using a surface-emission scheme. This can be done through fabrication of a second-order grating along the waveguide that out couples THz radiation vertically. In this case, the THz power is proportional to the top emitting area of the device $L_x L_y$ [see Fig. 15(a)]. Furthermore, the large emitting area in surface-emitting devices results in a more directional THz output, in comparison with the edge-emitting devices. Surface-emitting DFB lasers with second-order gratings have been demonstrated for traditional mid- and far- IR QCLs [60]–[64] and for intracavity second-harmonic generation in QCLs [65]. Here, we will discuss our preliminary investigation [66] of applying this concept to our devices to extract THz radiation through the waveguide surface.

Surface emission is achieved using a second-order grating for the THz wave. We, however, note that there is an important difference between our surface-emitting THz sources and the surface-emitting DFB QCLs with second-order gratings demonstrated previously [60]–[64]. The second-order gratings implemented for standard QCLs [60]–[64] matched the wave vector of a given laser mode, whereas in our devices, the grating should match the wave vector of the nonlinear polarization at the difference frequency, as shown later. Previously, second-order gratings in QCLs with intracavity second-harmonic generation also acted simultaneously as a DFB cavity for the laser mode

at the fundamental frequency [65]. This resulted in single-mode emission for all these devices. For the devices reported in this paper, only a second-order grating for the THz DFG wave can act as a very-high-order DFB grating for the mid-IR modes (approximately 12-order and 10-order gratings for the mid-IR pump beams in our case). In addition, the spatial extent of the THz mode is much larger than that of the mid-IR modes and the second-order grating for THz emission in our device thus has little interaction with the mid-IR laser modes [see Fig. 15(b)]. The grating coupling strength to the mid-IR modes is therefore poor, and as a result, multimode mid-IR and THz emission spectra are expected for our devices. We note that single-mode lasing can still be achieved in these devices by implementing DFB gratings for the mid-IR modes in addition to a second-order grating for the THz field.

The THz radiation in our devices is generated by the nonlinear polarization $P^{(2)}$ induced by the two mid-IR pumps in the QCL active region with nonlinear susceptibility $\chi^{(2)}$ [28], [31]. We can express $P^{(2)}$ as

$$P^{(2)}\left(x,y,z,t\right) = \varepsilon_0 \chi^{(2)}\left(x,z\right) E_{\omega_1}^z\left(x,z\right) E_{\omega_2}^z\left(x,z\right)$$
$$\times e^{-i\left(\left(\omega_1 - \omega_2\right)t - \left(k_1 - k_2\right)y\right)} \qquad (9)$$

where the z-direction is perpendicular to the waveguide layers, the y-direction is along the waveguide [see Fig. 15(a)], and $E_{\omega_1}^z\left(x,z\right)$ and $E_{\omega_2}^z\left(x,z\right)$ are the z-components of the electric field amplitudes of the two mid-IR waves at frequencies ω_1 and
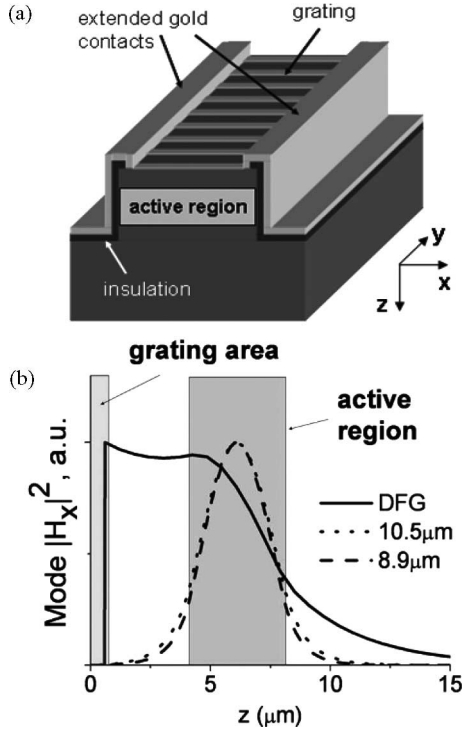
(a)

(b)

Fig. 15. (a) Schematic drawing of the ridge waveguide structure with the gold grating on top. (b) Magnetic field intensity in the TM_{00} waveguide mode for $\lambda = 8.9\,\mu$m, $\lambda = 10.5\,\mu$m, and $\lambda = 60\,\mu$m. The position of the active region and depth of the grating grooves ($\sim$300 nm) are indicated in gray. The grating is etched through the top plasmon layer and 100 nm into the lower doped top InP cladding layer.

ω_2, respectively. The propagation wave vector for a THz mode $H(x, y, z, t)$ generated by $P^{(2)}$ in a QCL waveguide equals to that of $P^{(2)}$ [28], [31]. $H(x, y, z, t)$ is given by

$$H(x, y, z, t) \sim \frac{\varepsilon_0 \omega}{2} \times \frac{e^{-i((\omega_1 - \omega_2)t - (k_1 - k_2)y)}}{i(k - (k_1 - k_2)) + \alpha/2}. \quad (10)$$

For efficient diffraction, outcoupling of the THz mode in a QCL waveguide into the radiation emitted from the surface, the grating wave vector must be chosen to match the wave vector of the THz wave in the QCL waveguide. In the case of our devices, effective modal indexes for the mid-IR laser modes at wavelengths $\lambda_1 \approx 8.9\,\mu$m and $\lambda_2 \approx 10.5\,\mu$m were calculated using COMSOL and found to be equal to ≈ 3.19 and ≈ 3.176, respectively. This corresponds to $k_1 - k_2 = k_g \approx 3515\,\text{cm}^{-1}$ and $2\pi/k_g \approx 17.9\,\mu$m, which was chosen to be the grating period of the reported devices.

A slight mismatch between the grating wave vector and that of the THz wave in a QCL waveguide will result in a surface-emission wave propagating at a slight angle to the grating surface normal with a nonzero horizontal wave vector component $k_y = k_1 - k_2 - k_g$. The output power should be only weakly dependent on this mismatch. The diffraction efficiency and therefore the output power, however, are sensitive to the waveguide and grating geometry. We are currently performing systematic studies of the diffraction efficiency for different device geometries, and the results will be published elsewhere.

The active region and waveguide structure of the QCL material used in this paper are described before. The devices were processed into surface-emitting ridge waveguide lasers with a grating on top of the ridges. The processing started with reactive ion etching (RIE) of the 28-μm-wide ridges using an Si nitride mask deposited via chemical vapor deposition. After this, a 300-nm-thick Si nitride insulation layer was deposited conformally and patterned on top of the ridge. The metal (Ti/Au 5 nm/200 nm)/air grating was defined by liftoff on top of the ridges to form the structures shown in Fig. 15(a). Finally, 300 nm of the top waveguide cladding was removed in the grating openings using RIE, with the metal grating acting as a mask. The current in our devices is injected though the sides of the ridge [see Fig. 15(a)] [67]. After the processing, the wafers were thinned to approximately 250 μm and cleaved into approximately 1-mm-long laser bars. The laser bars were indium mounted on copper heat sinks and the lasers were wire-bonded. Finally, a high-reflection (HR) coating (Al_2O_3/Ti/Au) was deposited on the back facets of the devices to improve their performance.

For measurement, the devices were operated in pulsed mode with 60 ns pulses at a 250-kHz repetition rate. The optical characterization was performed with the same setup as used for edge-emitting THz sources. Fig. 16(a) and (b) shows the mid-IR and THz spectra of a typical device, taken at 80 K. The positions of the peaks in the THz spectrum correspond to the frequency difference between the peaks in the mid-IR spectrum. Fig. 16(c) and (d) shows the L–I characteristics for the mid-IR and THz light at 80 K. The maximum mid-IR output power from a 1-mm-long device at 80 K was measured to be 3.5 W. The maximum THz output power from the surface was measured to be $\sim$1 μW (corrected for approximately $\sim$10% collection efficiency of our THz setup). The detected output power from the uncoated facet was a factor of 4 lower. We measured several devices and found the ratio of surface to facet emission to be in the range 2–5. The total power, however, varied significantly, which can be related back to the appearance of higher order modes in the 8.9 μm pump beam. The THz intensity decreased with decreasing power of the mid-IR pump beams. Both mid-IR modes were still observed at room temperature with a combined power of about 700 mW. The DFG signal ($\sim$70 nW), however, was too weak for spectral characterization. At the present stage, these devices have lower THz output power than normal ridge lasers with an Si hyperhemispherical lens attached to the device facet (see Fig. 14). However, the use of gratings is potentially more promising as it allows extraction of the THz radiation from the whole length of the device. We now plan to improve of the waveguide design of these devices to enhance the surface emission efficiency, and perform a systematic experimental study of the influence of the grating period, and other grating parameters such as duty cycle and grove depth, on the surface emission efficiency.

Overall, while the THz DFG QCL sources presented here provide less THz power than the THz QCLs discussed in Sections II and III, they do operate at room temperature. For the edge-emitting THz DFG QCL sources, the measured mid-IR to THz conversion efficiency is approximately 5 μW/W^2. Since mid-IR QCLs with CW power output levels of 1.5 W at room temperature have already been demonstrated [18], it appears that
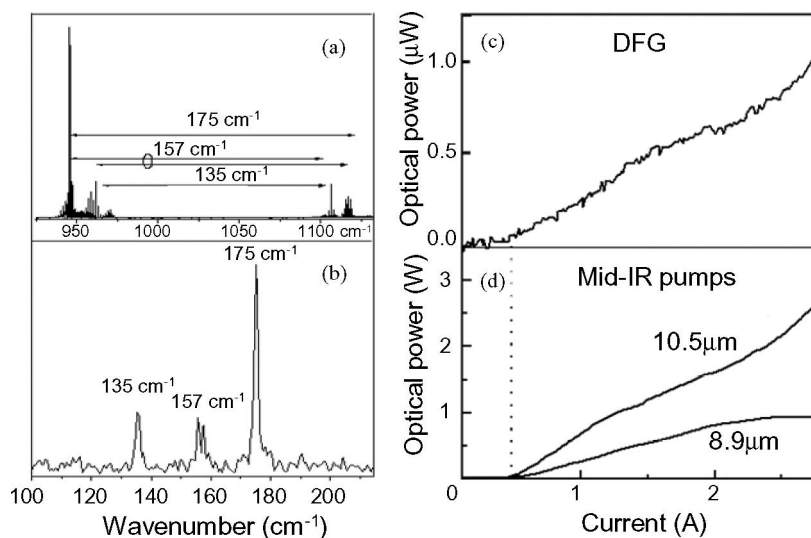
Fig. 16.   (a) Mid-IR emission spectrum collected from the edge of a typical device with second-order grating operated in pulsed mode at 80 K. (b) THz emission spectrum from the surface of the same device. (c) and (d) *L–I* characteristics of the device in (a) for the THz signal (c) and the two mid-IR pump beams (d), measured in pulsed mode at 80 K.

a THz QCL source with microwatt-level CW THz output power at room temperature is within reach. Further device optimization, including the utilization of an efficient surface-emission scheme for THz radiation extraction, may then lead to narrowband THz DFG QCLs providing up to a milliwatt of THz output power at room temperature. This output power is sufficient for high-resolution spectroscopy, and these sources may potentially be used as local oscillators for heterodyne detection [68], [69].

V. Conclusion

We have reviewed recent efforts to develop QCL sources suitable for room-temperature operation in the THz spectral region. Using conventional THz QCL technology, based on state-of-the-art GaAs/AlGaAs heterostructures, progress in increasing the operating temperature has been slow over the past few years. The active region and waveguide designs yielding the highest operating temperatures (178 K) to date have been presented and analyzed. We then discussed several processes leading to the deterioration of laser performance with temperature. The current maximum operating temperatures of THz QCLs are slowly approaching the temperature range accessible with thermoelectric coolers; therefore, one can hope that noncryogenic operation of THz QCLs will be achieved by further evolutionary improvement in laser design and structural quality.

We also discussed novel concepts for producing room-temperature, electrically-driven THz semiconductor sources that do not require population inversion across the THz laser transition. In particular, nonlinear optical interactions such as DFG or four-wave mixing processes are fairly insensitive to temperature, and can be implemented within a semiconductor crystal to yield a compact device. We have recently demonstrated room-temperature THz generation utilizing resonantly enhanced intracavity DFG within the active region of a mid-IR

QCL. The THz DFG power was low: microwatt levels at liquid nitrogen temperatures and around 0.3 μW at room temperature. However, the observed fall in the THz power with temperature was entirely due to a decrease in the mid-IR pump power, while the DFG efficiency stayed constant with temperature. There is plenty of room for improvement in the DFG efficiency and output power, through increase in the coherence length, the use of higher pump powers, and radiation extraction through a surface grating, *inter alia*. Achieving milliwatt THz powers at room temperature through DFG processes thus seems to be a realistic future goal.

References

[1] D. M. Mittleman, M. Gupta, R. Neelamani, R. G. Baraniuk, J. V. Rudd, and M. Koch, "Recent advances in terahertz imaging," *Appl. Phys. B*, vol. 68, pp. 1085–1094, 1999.

[2] P. H. Siegel, "Terahertz technology," *IEEE Trans. Microw. Theory Tech.*, vol. 50, no. 3, pp. 910–928, Mar. 2002.

[3] M. Tonouchi, "Cutting-edge terahertz technology," *Nature Photon.*, vol. 1, pp. 97–105, 2007.

[4] E. Gornik and A. A. Andronov, "Special issue—Far-infrared semiconductor lasers," *Opt. Quantum Electron.*, vol. 23, pp. S111–S349, 1991.

[5] R. Koehler, A. Tredicucci, F. Beltram, H. E. Beere, E. H. Linfield, A. G. Davies, D. A. Ritchie, R. C. Iotti, and F. Rossi, "Terahertz semiconductor heterostructure laser," *Nature*, vol. 417, pp. 156–159, 2002.

[6] J. Faist, F. Capasso, D. L. Sivco, A. L. Hutchinson, and A. Y. Cho, "Quantum cascade laser," *Science*, vol. 264, pp. 553–556, 1994.

[7] B. S. Williams, "Terahertz quantum-cascade lasers," *Nature Photon.*, vol. 1, pp. 517–525, 2007.

[8] B. S. Williams, S. Kumar, and Q. Hu, "Operation of terahertz quantum-cascade lasers at 164 K in pulsed mode and at 117 K in continuous-wave mode," *Opt. Exp.*, vol. 13, pp. 3331–3339, 2005.

[9] B. S. Williams, S. Kumar, H. Callebaut, and Q. Hu, "Terahertz quantum-cascade lasers operating up to 137 K," *Appl. Phys. Lett.*, vol. 83, pp. 5142–5144, 2003.

[10] B. S. Williams, S. Kumar, Q. Qin, Q. Hu, and J. L. Reno, "Terahertz quantum cascade lasers with double-resonant-phonon depopulation," *Appl. Phys. Lett.*, vol. 88, pp. 261101-1–261101-3, 2006.

[11] H. Luo, S. R. Laframboise, Z. R. Wasilewski, G. C. Aers, H. C. Liu, and J. C. Cao, "Terahertz quantum-cascade lasers based on a three-well active module," *Appl. Phys. Lett.*, vol. 90, pp. 041112-1–041112-3, 2007.

[12] M. A. Belkin, J. A. Fan, S. Hormoz, F. Capasso, S. P. Khanna, M. Lachab, A. G. Davies, and E. H. Linfield, "Terahertz quantum cascade lasers with metal–metal copper waveguides operating up to 178 K," *Opt. Exp.*, vol. 16, pp. 3242–3248, 2008.

[13] G. Scalari, L. Ajili, J. Faist, H. Beere, E. H. Linfield, D. Ritchie, and G. Davies, "Far-infrared ($\lambda \sim 87\ \mu$m) bound-to-continuum quantum-cascade lasers operating up to 90 K," *Appl. Phys. Lett.*, vol. 82, pp. 3165–3167, 2003.

[14] G. Scalari, N. Hoyler, M. Giovannini, and J. Faist, "Terahertz bound-to-continuum quantum cascade lasers based on optical-phonon scattering extraction," *Appl. Phys. Lett.*, vol. 86, pp. 181101-1–181101-3, 2005.

[15] C. Walther, M. Fischer, G. Scalari, R. Terazzi, N. Hoyler, and J. Faist, "Quantum cascade lasers operating from 1.2 to 1.6 THz," *Appl. Phys. Lett.*, vol. 91, pp. 131122-1–131122-3, 2007.

[16] L. Ajili, G. Scalari, N. Hoyler, M. Giovannini, and J. Faist, "InGaAs-AlInAs/InP terahertz quantum cascade laser," *Appl. Phys. Lett.*, vol. 87, pp. 141107-1–141107-3, 2005.

[17] M. Beck, D. Hofstetter, T. Aellen, J. Faist, U. Oesterle, M. Llegems, E. Gini, and H. Melchior, "Continuous wave operation of a mid-infrared semiconductor laser at room temperature," *Science*, vol. 295, pp. 201–305, 2002.

[18] A. Lyakh, C. Pflügl, L. Diehl, Q. J. Wang, Federico Capasso, X. J. Wang, J. Y. Fan, T. Tanbun-Ek, R. Maulini, A. Tsekoun, R. Go, C. Kumar, and N. Patel, "1.6 W high wall plug efficiency, continuous-wave room temperature quantum cascade laser emitting at 4.6 μm," *Appl. Phys. Lett.*, vol. 92, pp. 021103-1–021103-3, 2008.

[19] Y. Bai, S. Slivken, S. R. Darvish, and M. Razeghi, "Room temperature continuous wave operation of quantum cascade lasers with 12.5% wall plug efficiency," *Appl. Phys. Lett.*, vol. 93, p. 021103-1, 2008.

[20] J. Faist, F. Capasso, C. Sirtori, D. L. Sivco, A. L. Hutchinson, and A. Y. Cho, "Continuous-wave operation of a vertical transition quantum cascade laser above T = 80 K," *Appl. Phys. Lett.*, vol. 67, pp. 3057–3059, 1995.

[21] J. Faist, F. Capasso, C. Sirtori, D. L. Sivco, J. N. Baillargeon, A. L. Hutchinson, S.-N. G. Chu, and A. Y. Cho, "High power mid-infrared ($\lambda \sim 5\ \mu$m) quantum cascade lasers operating above room temperature," *Appl. Phys. Lett.*, vol. 68, pp. 3680–3682, 1996.

[22] D. Indjin, Z. Ikonic, V. D. Jovanovic, N. Vukmirovic, P. Harrison, and R. W. Kelsall, "Relationship between carrier dynamics and temperature in terahertz quantum cascade structures: Simulation of GaAs/AlGaAs, SiGe/Si and GaN/AlGaN devices," *Semicond. Sci. Technol.*, vol. 20, pp. S237–S245, 2005.

[23] G. Sun, R. A. Soref, and J. B. Khurgin, "Active region design of a terahertz GaN/Al$_{0.15}$Ga$_{0.85}$N quantum cascade laser," *Superlattices Microstruct.*, vol. 37, pp. 107–113, 2005.

[24] G. Dehlinger, L. Diehl, U. Gennser, H. Sigg, J. Faist, K. Ensslin, D. Grützmacher, and E. Müller, "Intersubband electroluminescence from silicon-based quantum cascade structures," *Science*, vol. 290, pp. 2277–2280, 2000.

[25] L. Diehl, S. Menteşe, E. Müller, D. Grützmacher, H. Sigg, U. Gennser, I. Sagnes, Y. Campidelli, O. Kermarrec, D. Bensahel, and J. Faist, "Electro-luminescence from strain-compensated Si$_{0.2}$Ge$_{0.8}$/Si quantum-cascade structures based on a bound-to-continuum transition," *Appl. Phys. Lett.*, vol. 81, pp. 4700–4702, 2002.

[26] S. A. Lynch, R. Bates, D. J. Paul, D. J. Norris, A. G. Cullis, Z. Ikonic, R. W. Kelsall, P. Harrison, D. D. Arnone, and C. R. Pidgeon, "Intersubband electroluminescence from Si/SiGe cascade emitters at terahertz frequencies," *Appl. Phys. Lett.*, vol. 81, pp. 1543–1545, 2002.

[27] N. S. Wingreen and C. A. Stafford, "Quantum-dot cascade laser: Proposal for an ultralow-threshold semiconductor laser," *IEEE J. Quantum Electron.*, vol. 33, no. 7, pp. 1170–1173, Jul. 1997.

[28] Y. R. Shen, *The Principles of Nonlinear Optics*. New York: Wiley, 1984.

[29] T. Tanabe, K. Suto, and J. Nishizawa, "Frequency-tunable terahertz wave generation via excitation of phonon-polaritons in GaP," *J. Phys. D, Appl. Phys.*, vol. 36, pp. 953–957, 2003.

[30] K. L. Vodopyanov, M. M. Fejer, X. Yu, J. S. Harris, Y.-S. Lee, W. C. Hurlbut, V. G. Kozlov, D. Bliss, and C. Lynch, "Terahertz-wave generation in quasi-phase-matched GaAs," *Appl. Phys. Lett.*, vol. 89, pp. 141119-1–141119-3, 2006.

[31] M. A. Belkin, F. Capasso, A. Belyanin, D. L. Sivco, A. Y. Cho, D. C. Oakley, C. J. Vineis, and G. W. Turner, "Terahertz quantum-cascade-laser source based on intracavity difference-frequency generation," *Nature Photon.*, vol. 1, pp. 288–292, 2007 (and supplementary information).

[32] M. A. Belkin, F. Capasso, F. Xie, A. Belyanin, M. Fischer, A. Wittmann, and J. Faist, "Room temperature terahertz quantum cascade laser source based on intra-cavity difference-frequency generation," *Appl. Phys. Lett.*, vol. 92, pp. 201101-1–201101-3, 2008.

[33] K. Unterrainer, R. Colombelli, C. Gmachl, F. Capasso, H. Y. Hwang, A. M. Sergent, D. L. Sivco, and A. Y. Cho, "Quantum cascade lasers with double metal-semiconductor waveguide resonators," *Appl. Phys. Lett.*, vol. 80, pp. 3060–3062, 2002.

[34] S. Kohen, B. S. William, and Q. Hu, "Electromagnetic modeling of terahertz quantum cascade laser waveguides and resonators," *J. Appl. Phys.*, vol. 97, pp. 053106-1–053106-9, 2005.

[35] M. A. Ordal, R. J. Bell, R. W. Alexander, Jr., L. L. Long, and M. R. Querry, "Optical properties of fourteen metals in the infrared and far infrared: Al, Co, Cu, Au, Fe, Pb, Mo, Ni, Pd, Pt, Ag, Ti, V and W," *Appl. Opt.*, vol. 24, pp. 4493–4499, 1985.

[36] M. Born and E. Wolf, *Principles of Optics*. Cambridge, U.K.: Cambridge Univ. Press, 1999.

[37] D. R. Lide, Ed., "Electrical resistivity of pure metals," in *CRC Handbook of Chemistry and Physics (Internet Version 2008)*, 88th ed. Boca Raton, FL/New York: CRC Press/Taylor & Francis, 2008.

[38] H. Callebaut, S. Kumar, B. S. Williams, Q. Hu, and J. L. Reno, "Importance of electron-impurity scattering for electron transport in terahertz quantum-cascade lasers," *Appl. Phys. Lett.*, vol. 84, pp. 645–647, 2004.

[39] H. Callebaut and Q. Hu, "Importance of coherence for electron transport in terahertz quantum cascade lasers," *J. Appl. Phys.*, vol. 90, pp. 104505-1–104505-11, 2005.

[40] D. Indjin, Z. Ikonic, V. D. Jovanovic, P. Harrison, and R. W. Kelsall, "Mechanisms of carrier transport and temperature performance evaluation in terahertz quantum cascade lasers," *Semicond. Sci. Technol.*, vol. 19, pp. S104–S106, 2004.

[41] C. Jirauschek, G. Scarpa, P. Lugli, M. S. Vitiello, and G. Scamarcio, "Comparative analysis of resonant phonon THz quantum cascade lasers," *J. Appl. Phys.*, vol. 101, pp. 086109-1–086109-3, 2007.

[42] H. Li, J. C. Cao, J. T. Lu, and Y. J. Han, "Monte Carlo simulation of extraction barrier width effects on terahertz quantum cascade lasers," *Appl. Phys. Lett.*, vol. 92, pp. 221105-1–221105-3, 2008.

[43] R. Ferreira and G. Bastard, "Evaluation of some scattering times for electrons in unbiased and biased single- and multiple-quantum-well structures," *Phys. Rev. B*, vol. 40, pp. 1074–1086, 1989.

[44] J. Faist, C. Sirtori, F. Capasso, L. N. Pfeiffer, K. W. West, D. L. Sivco, and A. Y. Cho, "Quantum cascade lasers," in *Intersubband Transitions in Quantum Wells: Physics and Device Applications II*, H. C. Liu and F. Capasso, Eds. San Diego, CA: Academic, 2000.

[45] J. H. Smet, C. G. Fonstad, and Q. Hu, "Intrawell and interwell intersubband transitions in multiple quantum wells for far-infrared sources," *J. Appl. Phys.*, vol. 79, pp. 9305–9307, 1996.

[46] M. S. Vitiello, G. Scamarcio, V. Spagnolo, B. S. Williams, S. Kumar, and Q. Hu, "Measurement of subband electronic temperatures and population inversion in THz quantum-cascade lasers," *Appl. Phys. Lett.*, vol. 86, pp. 111115-1–111115-3, 2005.

[47] L. Ajili, G. Scalari, M. Giovannini, N. Hoyler, and J. Faist, "Doping in quantum cascade lasers. II. GaAs/Al$_{0.15}$Ga$_{0.85}$As terahertz devices," *J. Appl. Phys.*, vol. 100, pp. 043102-1–043102-3, 2006.

[48] H. C. Liu, M. Wachter, D. Ban, Z. R. Wasilewski, M. Buchanan, G. C. Aers, J. C. Cao, S. L. Feng, B. S. Williams, and Q. Hu, "Effect of doping concentration on the performance of terahertz quantum-cascade lasers," *Appl. Phys. Lett.*, vol. 87, pp. 141102-1–141102-3, 2005.

[49] H. Luo, S. R. Laframboise, Z. R. Wasilewski, and H. C. Liu, "Effects of injection barrier on performance of terahertz quantum-cascade lasers," *Electron. Lett.*, vol. 43, pp. 633–634, 2007.

[50] H. Luo, S. R. Laframboise, Z. R. Wasilewski, H. C. Liu, and J. C. Cao, "Effects of extraction barrier width on performance of terahertz quantum-cascade lasers," *Electron. Lett.*, vol. 44, pp. 630–631, 2008.

[51] J. Faist, D. Hofstetter, M. Beck, T. Aellen, M. Rochat, and S. Blaser, "Bound-to-continuum and two-phonon resonance quantum-cascade lasers for high duty cycle, high temperature operation," *IEEE J. Quantum Electron.*, vol. 38, no. 6, pp. 533–546, Jun. 2002.

[52] C. Gmachl, A. Belyanin, D. L. Sivco, M. L. Peabody, N. Owschimikow, A. M. Sergent, F. Capasso, and A. Y. Cho, "Optimized second-harmonic generation in quantum cascade lasers," *IEEE J. Quantum Electron.*, vol. 39, no. 11, pp. 1345–1355, Nov. 2003.

[53] M. M. Fejer, S. J. B. Yoo, R. L. Byer, A. Harwit, and J. S. Harris, Jr., "Observation of extremely large quadratic susceptibility at 9.6–10.8 μm in electric field biased AlGaAs/GaAs quantum wells," *Phys. Rev. Lett.*, vol. 62, pp. 1041–1044, 1989.

[54] F. Capasso, C. Sirtori, and A. Y. Cho, "Coupled quantum well semiconductors with giant electric field tunable nonlinear optical properties in the infrared," *IEEE J. Quantum Electron.*, vol. 30, no. 5, pp. 1313–1326, 1994.

[55] E. Rosencher, A. Fiore, B. Vinter, V. Berger, P. Bois, and J. Nagle, "Quantum engineering of optical nonlinearities," *Science*, vol. 271, pp. 168–173, 1996.

[56] C. Sirtori, F. Capasso, J. Faist, L. N. Pfeiffer, and K. W. West, "Far-infrared generation by doubly resonant difference frequency mixing in a coupled quantum well two-dimensional electron gas system," *Appl. Phys. Lett.*, vol. 65, pp. 445–447, 1994.

[57] E. Dupont, Z. R. Wasilewski, and H. C. Liu, "Terahertz emission in asymmetric quantum wells by frequency mixing of midinfrared waves," *IEEE J. Quantum Electron.*, vol. 42, no. 11, pp. 1157–1174, Nov. 2006.

[58] C. Gmachl, F. Capasso, D. L. Sivco, and A. Y. Cho, "Recent progress in quantum cascade lasers and applications," *Rep. Prog. Phys.*, vol. 64, pp. 1533–1601, 2001.

[59] A. W. M. Lee, Q. Qin, S. Kumar, B. S. Williams, Q. Hu, and J. L. Reno, "High-power and high-temperature THz quantum-cascade lasers based on lens-coupled metal–metal waveguides," *Opt. Lett.*, vol. 32, pp. 2840–2842, 2007.

[60] D. Hofstetter, J. Faist, M. Beck, and U. Oesterle, "Surface-emitting 10.1 μm quantum-cascade distributed feedback lasers," *Appl. Phys. Lett.*, vol. 75, pp. 3769–3771, 1999.

[61] C. Pflügl, M. Austerer, W. Schrenk, S. Golka, G. Strasser, R. P. Green, L. R. Wilson, J. W. Cockburn, A. B. Krysa, and J. S. Roberts, "Single-mode surface-emitting quantum-cascade lasers," *Appl. Phys. Lett.*, vol. 86, pp. 211102-1–211102-3, 2005.

[62] O. Demichel, L. Mahler, T. Losco, C. Mauro, R. Green, J. H. Xu, A. Tredicucci, F. Beltram, H. E. Beere, D. A. Richie, and V. Tamosiunas, "Surface plasmon photonic structures in terahertz quantum cascade lasers," *Opt. Exp.*, vol. 14, pp. 5335–5345, 2006.

[63] J. A. Fan, M. A. Belkin, F. Capasso, S. Khanna, M. Lachab, A. G. Davies, and E. H. Linfield, "Surface emitting terahertz quantum cascade laser with a double-metal waveguide," *Opt. Exp.*, vol. 14, pp. 11672–11680, 2006.

[64] S. Kumar, B. S. Williams, Q. Qin, A. W. M. Lee, Q. Hu, and J. Reno, "Surface-emitting distributed feedback terahertz quantum-cascade lasers in metal–metal waveguides," *Opt. Exp.*, vol. 15, pp. 113–128, 2007.

[65] M. Austerer, C. Pflügl, S. Golka, W. Schrenk, A. M. Andrews, T. Roch, and G. Strasser, "Coherent 5.35 μm surface emission from a GaAs-based distributed feedback quantum-cascade laser," *Appl. Phys. Lett.*, vol. 88, pp. 121104-1–121104-3, 2006.

[66] C. Pflugl, M. A. Belkin, Q. J. Wang, M. Geiser, A. Belyanin, M. Fischer, A. Wittmann, J. Faist, and F. Capasso, "Surface-emitting terahertz quantum cascade laser source based on intracavity difference-frequency generation," *Appl. Phys. Lett.*, vol. 93, pp. 161110-1–161110-3, 2008.

[67] D. Hofstetter, J. Faist, M. Beck, and U. Oesterle, "Sufrace-emitting 10.1 μm quantum-cascade distributed feedback lasers," *Appl. Phys. Lett.*, vol. 75, pp. 3769–3771, 1999.

[68] S. Barbieri, J. Alton, H. E. Beere, E. H. Linfied, D. A. Ritchie, S. Withington, G. Scalari, L. Ajili, and J. Faist, "Heterodyne mixing of two far-infrared quantum cascade lasers by use of a point-contact Schottky diode," *Opt. Lett.*, vol. 29, pp. 1632–1634, 2004.

[69] J. R. Gao, J. N. Hovenier, Z. Q. Yang, J. J. A. Baselmans, A. Baryshev, M. Hajenius, T. M. Klapwijk, A. J. L. Adam, T. O. Klaassen, B. S. Williams, S. Kumar, Q. Hu, and J. L. Reno, "Terahertz heterodyne receiver based on a quantum cascade laser and a superconducting bolometer," *Appl. Phys. Lett.*, vol. 86, pp. 244104-1–244104-3, 2005.

Mikhail A. Belkin (M'07) received the B.S. degree in physics and mathematics from Moscow Institute of Physics and Technology, Moscow, Russia, in 1998, and the Ph.D. degree in physics from the University of California, Berkeley, in 2004.

From 2004 to 2006, he was a Postdoctoral Fellow in the School of Engineering and Applied Sciences, Harvard University, where he was a Research Associate from 2006 to 2008. He is currently an Assistant Professor in the Department of Electrical and Computer Engineering, University of Texas at Austin. His current research interests include novel midinfrared and terahertz (THz) quantum cascade laser sources, optical nonlinearities in semiconductor nanostructures, midinfrared and THz photonic and plasmonic systems for chemical sensing, and metamaterials.
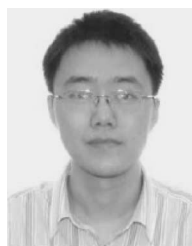
Qi Jie Wang was born in Liaoning, China, in 1979. He received the B.E. degree in electrical engineering from the University of Science and Technology of China (USTC), Hefei, China, in 2001, and the Ph.D. degree in electrical and electronic engineering from Nanyang Technological University, Nanyang, Singapore, in 2005.

Since January 2007, he has been a Postdoctoral Researcher in the School of Engineering and Applied Science, Harvard University, Cambridge, MA. His current research interests include midinfrared and terahertz quantum cascade lasers, nanotechnology, fiber optics and photonics, optical communications, systems, and signal processing.

Dr. Wang was the recipient of the Top Prize for the Young Inventor Awards of the International Society for Optical Engineering (SPIE) Photonics Europe Innovation Village in 2004, the Golden Award from the Fifth Young Inventor's Awards in 2005, the Institution of Engineers Singapore (IES) Prestigious Engineering Achievement Award 2005 of Singapore, and the 2005 Singapore Millennium Foundation (SMF) Fellowship.

Christian Pflügl received the Diploma in physics from the University of Regensburg, Regensburg, Germany, in 2001, and the Ph.D. degree in electrical engineering from Vienna University of Technology, Vienna, Austria, in 2005.

From 2005 to 2006, he was a Postdoctoral Researcher at Vienna University of Technology, where he was engaged in research on quantum cascade lasers. In 2006, he joined the Group of Federico Capasso, Harvard University, Cambridge, MA. His current research interests include high-performance and single-mode quantum cascade lasers as well as the physics of these devices, nonlinear optics, midinfrared plasmonics, microfabrication, and nanotechnology.

Alexey Belyanin received the Ph.D. degree in physics from the Institute of Applied Physics, Russian Academy of Sciences, Nizhny Novgorod, Russia, in 1995.

He was engaged in research on ultrafast coherent optical processes in semiconductors, quantum electrodynamics (QED) processes in magnetized plasma, and high-energy astrophysics. In 1999, he joined the Department of Physics, Texas A&M University, College Station, where he is currently an Associate Professor. His current research interests include ultrafast and nonlinear optics of semiconductor nanostructures, and physics of optoelectronic devices. He has authored or coauthored more than 100 scientific papers.

Dr. Belyanin is a member of the American Physical Society, the Optical Society of America, the International Society for Optical Engineering (SPIE), and the International Committee on Space Research (COSPAR). He was the recipient of the Jo Ann Treat Award in 2007, the National Science Foundation (NSF) CAREER Award in 2006, and the President of Russian Federation Award for Outstanding Young Scientists in 1996.

Suraj P. Khanna received the B.Eng. degree (first class) in electronics and telecommunications engineering from the University of Amravati, Amravati, India, in 2001, and the M.Sc. degree in nanoscale science and technology and the Ph.D. degree in electronic and electrical engineering from the University of Leeds, Leeds, U.K., in 2004 and 2008, respectively.

Since 2008, he has been a Postdoctoral Research Associate at the University of Leeds. His current research interests include molecular beam epitaxial growth, semiconductor device fabrication, quantum cascade lasers, and terahertz-frequency optical systems.

Alexander Giles Davies received the B.Sc. (Hons.) degree (first class) in chemical physics from the University of Bristol, Bristol, U.K., in 1987, and the Ph.D. degree in semiconductor physics from the Cavendish Laboratory, University of Cambridge, Cambridge, U.K., in 1991.

He was an Australian Research Council Postdoctoral Research Fellow at the University of New South Wales, Sydney, Australia, for three years. During 1995, he was the Royal Society University Research Fellow at the University of Cambridge. In 2002, he was the Chair of Electronic and Photonic Engineering, University of Leeds, Leeds, U.K., where he is currently the Director of Research and the Deputy Head of the School of Electronic and Electrical Engineering. His current research interests include semiconductor nanostructures, terahertz-frequency optics and electronics, and bionanotechnology. He is an Associate Editor of the *Philosophical Transactions of the Royal Society*.

Edmund Harold Linfield received the B.A. (Hons.) degree in physics and the M.A. degree from the University of Cambridge, Cambridge, U.K., in 1986 and 1991, respectively, and the Ph.D. degree in semiconductor physics from the Cavendish Laboratory, University of Cambridge, in 1991.

He was a Postdoctoral Researcher Associate at the Cavendish Laboratory, University of Cambridge, where he was appointed as an Assistant Director of Research in 1997. He was the Fellow of Gonville and Caius College, Cambridge. In 2004, he was the Chair of Terahertz Electronics at the University of Leeds, Leeds, U.K., where he is currently the Director of the Institute of Microwaves and Photonics. His current research interests include semiconductor growth and device fabrication, terahertz-frequency optics and electronics, and nanotechnology.

Federico Capasso (M'79–SM'85–F'87) received the Ph.D. degree in physics (*summa cum laude*) from the University of Rome, Rome, Italy, in 1973.

From 1974 to 1976, he was with Fondazione Ugo Bordoni as a Researcher. In 1976, he joined Bell Laboratories, where he was a Member of the Technical Staff from 1977 to 1986, the Department Head from 1986 to 2000, and the Vice President for Physical Research from 2000 to 2002. In 1997, he was made a Bell Labs Fellow for his scientific contributions. He is currently the Robert Wallace of Applied Physics and the Vinton Hayes Senior Research Fellow in Electrical Engineering at Harvard University, Cambridge, MA. He has been engaged in basic and applied research on the design of new artificial materials and devices, using an approach he pioneered known as band structure engineering, in investigations on quantum electrodynamical phenomena such as the Casimir effect and on surface plasmon photonics. He is a coinventor of the quantum cascade laser, a fundamentally new light source, which has now been commercialized. His recent achievements include the invention and demonstration of low-divergence semiconductor lasers with plasmonic collimators, plasmonic laser antennas, and the first measurement of repulsive Casimir forces. He has authored or coauthored more than 300 papers, edited four volumes, and holds more than 55 U.S. Patents.

Dr. Capasso is a member of the National Academy of Sciences, the National Academy of Engineering, and an honorary member of the Franklin Institute. He is a Fellow of the American Academy of Arts and Sciences, the Optical Society of America (OSA), the American Physical Society, the International Society for Optical Engineering (SPIE), and the American Association for the Advancement of Science (AAAS). He has received the King Faisal International Prize for Science, the IEEE Edison Medal, the Arthur Schawlow Prize in Laser Science, the Wetherill Medal of the Franklin Institute, the Robert Wood Prize of the OSA, the William Streifer Award of the Laser and Electro-Optic Society (IEEE), the Rank Prize in Optoelectronics (U.K.), the IEEE David Sarnoff Award in Electronics, the Duddell Medal of the Institute of Physics (U.K.), the Willis Lamb Medal for Laser Science and Quantum Optics, the Materials Research Society Medal, the "Vinci of Excellence" Prize (France), the Welker Memorial Medal (Germany), the New York Academy of Sciences Award, the Newcomb Cleveland Prize of the American Association for the Advancement of Science, and the National Aeronautics and Space Administration (NASA) Achievement Award.